Strain-driven spin-state transition and superexchange interaction in LaCoO_{3}: Ab initio study

Hosung Seo, Agham Posadas, and Alexander A. Demkov

Phys. Rev. B **86**, 014430 — Published 26 July 2012

DOI: 10.1103/PhysRevB.86.014430

Strain-driven spin state transition and superexchange interaction in $LaCoO_3$: *Ab initio* study

Hosung Seo, Agham Posadas and Alexander A. Demkov[1]
Department of Physics, The University of Texas at Austin, Austin, Texas 78712, USA

Abstract

Using spin density functional theory with the Hubbard correction we investigate the magnetic structure of strained $LaCoO_3$. We show that beyond biaxial tensile strain of 2.5%, local magnetic moments originating from the high spin (HS) state of Co^{3+} emerge in a low spin (LS) Co^{3+} matrix. In contrast, we find that compressive strain is not able to stabilize a magnetic state due to geometric constraints. $LaCoO_3$ accommodates tensile strain *via* spin state disproportionation resulting in an unusual sublattice structure. In tensile-strained $LaCoO_3$, the first nearest neighbor (n.n.) exchange coupling is ferromagnetic (FM) while the second n.n. interaction is stronger and antiferromagnetic (AFM). This unusual feature of the exchange parameters is qualitatively verified with a model superexchange calculation. Due to the competition between the FM and AFM couplings in the system, we find that the most probable magnetic structure of tensile-strained LCO is a canted-spin structure, which may explain the relatively small observed magnetic moment of $0.7\mu_B/Co^{3+}$.

I. Introduction

Artificial heterostructures with functional perovskite oxides as building blocks can now be synthesized using advanced thin film deposition techniques [1]. Furthermore, strain engineering in these oxide heterostructures opens up routes for creating novel electronic phases [2-4]. An exciting example is the recent demonstration of biaxial tensile strain stabilizing an insulating ferromagnetic (FM) ground state in $LaCoO_3$ (LCO) [5-14]. Though LCO is a classic example of a correlated 3*d* transition metal perovskite oxide [15,16], FM correlation has never been observed for the bulk ground state where the Co^{3+} ions exist in the so-called low spin (LS) state (total spin per Co S=0) [15]. Since the first demonstration by Fuchs *et al.* using films grown by pulsed laser deposition (PLD) [5] and by our group using molecular beam epitaxy (MBE) [10], several intriguing properties of strained LCO have been found experimentally. In addition to transport measurements showing insulating behavior for tensile-strained FM LCO [7], Fuchs and co-workers have also shown that both the population of higher spin states and the magnetization in LCO increase as tensile strain increases [6]. Using X-ray techniques, Merz and co-workers have suggested that the magnetic structure of tensile-strained LCO grown on $SrTiO_3$ (STO) is a mixture of Co^{3+} high spin (HS) and Co^{3+} LS states [13]. A recent report by Metha *et al.* also suggests that compressive strain by itself cannot produce a FM state in LCO [12], indicating the existence of an asymmetric orbital-lattice interaction [4]. Magnetization measurements of compressively strained LCO on $LaAlO_3$ (LAO) substrates show only weak to no ferromagnetism [6,7,12]. Most recently, Sterbinsky *et al.* have shown that inter-site hybridization involving Co and O states in LCO on STO is weaker than that in LCO on LAO by comparing the pre-edge structure of the Co *K*-edge X-ray absorption spectra [14]. A complete theoretical picture of strained LCO must be able to account for all these experimental observations.

[1] demkov@physics.utexas.edu

The minimal theoretical model to describe the basic electronic properties of LCO is a $[CoO_6]^{9-}$ octahedron within the ligand field theory [16]. In a cubic crystal field, the localized 3*d* orbitals are split into doubly degenerate e_g (d_{z^2} and $d_{x^2-y^2}$) and triply degenerate t_{2g} (d_{xy}, d_{yz} and d_{zx}) states separated by the crystal field splitting 10*Dq*. Other important energy scales are the on-site Hubbard repulsion *U,* Hund's exchange coupling J_H, and the hopping matrix between the Co 3*d* and O 2*p* orbitals *t*. Due to all competing interactions being of the same order, Co^{3+} can access different spin states: low-spin (LS, $t_{2g}^6e_g^0$, S=0), intermediate-spin (IS, $t_{2g}^5e_g^1$, S=1), or high-spin (HS, $t_{2g}^4e_g^2$, S=2). The ground state is insulating and nonmagnetic (NM) with Co^{3+} in the LS state. LCO undergoes a crossover to a paramagnetic insulating phase at about 100 K, and a metal-insulator transition above 500 K [17]. However, the spin structure at different temperatures has been highly debated. For example, the LS-HS [17,18], LS-IS [19,20], and LS-HS/LS crossover scenarios have been discussed in the literature [21-25].

While a substantial body of experimental results for strained LCO has been reported, there is a clear lack of theoretical understanding taking into account all the experimental observations [10,26-28]. Using density functional theory (DFT), Gupta *et al.*, have claimed that tensile strain is able to stabilize a FM ground state in LCO [26] while Rondinelli *et al.*, have suggested that strain by itself cannot produce a FM state [27]. However, Coulomb correlation effects for the localized 3*d* orbitals in LCO have not been considered in Ref. [26] and proper structural optimization has not been performed in Ref. [27]. In our previous work, using local spin density approximation combined with the Hubbard *U* correction (LSDA+*U)*, we have shown that a ferromagnetic state based on a *homogenous* intermediate spin (IS) state (S=1) can be stabilized above 3.8% tensile strain [10]. The ferromagnetic IS state is, however, inconsistent with two experimentally determined properties of strained LCO: the IS state is half-metallic while experiment shows that strained LCO is insulating [7], and a rather high critical strain of 3.8% is required, which is somewhat higher than that in experiment (~2%) [5-10]. Most recently, using a LDA+*U* approach, Hsu *et al.* have shown that a HS/LS mixed state has a lower energy than that of the IS state in tensile-strained LCO on STO [28]. They have also suggested that the proposed HS/LS state is ferromagnetically coupled *via* superexchange interaction by considering the nearest neighbor interaction.

In this article, using first-principles calculations, we expand our previous theoretical work on strained LCO [10] by considering homogeneous IS states and inhomogeneous HS/LS mixed states as a function of biaxial strain from -4% to 4%. We show that beyond a tensile strain of 2.5%, LCO undergoes a spin state transition from LS to mixed HS/LS states [13], and also explain why the higher concentration of HS Co^{3+} is preferred in tensile-strained LCO [6]. This feature of our theory is due to a reduced mixing between the Co 3*d* and O 2*p* states in the HS CoO_6 units, leading to softer HS Co-O bonds, compared to that of the LS CoO_6 units [14]. The HS/LS state has an energy gap of 0.5 eV consistent with tensile-strained FM LCO being insulating [7]. On the other hand, we show that no magnetic state is stable under compressive strain [4,6,7,12].

To understand the FM ordering in tensile-strained LCO found in experiment, we calculate the first and second nearest neighbor (n.n.) exchange parameters in the 1:1 HS/LS state [29,30]. The qualitative feature of the exchange parameters is further verified within a model superexchange calculation. We show that the first n.n. coupling is ferromagnetic. On the other hand, the second n.n. coupling is strongly antiferromagnetic (AFM). As a result, we find that the most stable collinear magnetic structure of the

HS/LS state is not a FM structure, but an AFM one with a ↑↑↓↓ order along the *c*-direction. However, we remark that the energy difference between the FM and AFM solutions is very small (about 2~3 meV/Co^{3+}). Furthermore, we find that there are several noncollinear magnetic structures that are degenerate in energy with the collinear AFM solution. Moreover, noting that a small magnetic field is typically applied in experiment, we argue that a canted magnetic structure with a net magnetization could be stabilized.

The rest of the paper is organized as follows: in section 2, we explain the computational details; in section 3, we examine the stability of various magnetic configurations under epitaxial strain; in section 4, in order to explore the mechanism of strain-induced spin state transition in LCO, we discuss the electronic and structural response of LCO to applied strain, depending on its magnetic state; in section 5, we calculate the exchange parameters in the 1:1 HS/LS configuration and describe the superexchange paths using an effective e_g model; in section 6, we discuss a possible spin-canted magnetic structure of tensile-strained LCO; and in section 7, we summarize our main results.

II. Computational Details

The calculations are done using density functional theory as implemented in the VASP code [31] along with projector augmented wave pseudopotentials to describe La, Co and O [32] and a cutoff energy of 600 eV. The valence configurations for the elements are $5s^2 5p^6 5d^1 6s^2$ for La, $3d^7 4s^2$ for Co, and $2s^2 2p^4$ for O. Each self-consistent electronic calculation is converged to 10^{-6} eV/cell and the tolerance factor for the ionic relaxation is set to 0.01 eV/Å. We employ the local (spin) density approximation combined with the Hubbard *U* correction (LDA+*U*) in the rotationally invariant formalism [33,34] to describe the static electronic correlation effect of 3*d* electrons of the Co^{3+} ion. For the exchange-correlation energy part of the LDA functional, we use the Perdew-Zunger parameterization of the Ceperly-Alder data [35]. For the Hubbard *U* correction, we use the Dudarev formalism to describe the local moment formation in strained LCO applying U_{eff} (= *U* - *J*) of 3.8eV on the Co 3*d* orbitals. In addition, we check that the original Liechtenstein's rotationally invariant functional with *U* = 5.27 eV and *J* = 1.47 eV [36] gives qualitatively the same electronic structure for the HS/LS mixed states. The rationale for the *U* value is based on the following: (1) it is consistent with the existing photoemission and cluster calculation data (U ≈ 5~5.5 eV) [37-39]; (2) it produces a nonmagnetic semiconducting ground state with an energy gap of 0.7 eV, in good agreement with the experimental value of 0.6 ~ 0.9 eV [37,40]; and (3) the theoretical structure is in good agreement with experiment [41]. The ground state structure of LCO is shown in Fig. 1 (a). It is described with space group $R\bar{3}c$ with a distorted corner-sharing CoO_6 octahedral network ($a^-a^-a^-$ in the Glazer tilt system [42,43]). We compare the calculated structural parameters for bulk LCO with experiment in Table 1.

Motivated by the coherent cube-on-cube epitaxy of LCO with thickness of about 40 nm on STO [10,11], we consider pure strain effects by performing 'strained-bulk' calculations using supercells. To examine the stability of various magnetic states in tensile-strained LCO, we use three cell types: $\sqrt{2}\times\sqrt{2}\times 2$, $\sqrt{2}\times\sqrt{2}\times 4$, and 2×2×2 with respect to a five-atom pseudo-cubic cell, for which 6×6×4, 6×6×2, and 4×4×4 Monkhorst-Pack *k*-point grids are used for the Brillouin zone integration, respectively [44]. To describe the effect of strain on the electronic and magnetic properties of LCO, we use the $\sqrt{2}\times\sqrt{2}\times 2$ cell shown in Fig. 1 (b). We vary the in-plane lattice parameter a_T biaxially and optimize the *c*-axis lattice

constant and all internal degrees of freedom without any structural constraints. Strain is defined as $(a_T - a_{pc})/(a_{pc})$, where a_{pc} is the pseudo-cubic lattice parameter of non-magnetic (NM) LCO, which is calculated to be 3.74 Å. We consider biaxial strain levels in the range from -4% to 4%. The optimized *c* and cell volume of LCO with different magnetic states are shown in Fig. 2. The overall trend shown in Fig. 2 is that under tensile (compressive) strain, LCO tends to shrink (expand) in the *c* direction due to the Poisson effect while the cell volume increases (decreases) as a function of strain. Finally, to calculate the exchange coupling constants, we use 2×2×4 and 4×2×2 supercells, for which 4×4×2 and 2×4×4 *k*-point meshes are used, respectively.

III. Strain-induced Spin State Transition in $LaCoO_3$

We start our investigation by searching for the most stable magnetic solution in LCO on STO at low temperature (theoretical strain = 3.5%). We use $\sqrt{2}\times\sqrt{2}\times 2$, $\sqrt{2}\times\sqrt{2}\times 4$, and 2×2×2 cells for which the *c*-axis lattice constant and the internal structure are optimized for each magnetic configuration. We first test homogeneous magnetic configurations with all Co^{3+} in either the IS or HS states. For the homogeneous HS state, only an antiferromagnetically (AFM) aligned solution (*G*-type) is stabilized. This is consistent with the Goodenough-Kanamori-Anderson rule [45] stating that the indirect superexchange between half-filled orbitals, mediated by O 2*p* with an angle close to 180 degrees, is antiferromagnetic. At 3.5 % tensile-strain, however, the homogeneous IS state is still 15 meV/formula-unit higher in energy than the NM state with the homogeneous HS state 250 meV/formula-unit higher in energy than the IS state. Additionally, the homogeneous IS state is half-metallic, while experimentally, strained LCO shows an insulating behavior [7]. Therefore, we conclude that the homogeneous magnetic configurations are unlikely to be the magnetic structure of tensile-strained LCO.

We next consider mixed magnetic configurations where HS Co^{3+} ions are embedded in a LS Co^{3+} matrix. We compare the total energy of *twenty two different* HS/LS configurations, where various geometric arrangements of HS Co^{3+} ions are considered. We have also compared various FM- and AFM-ordered states. However, we find that the dominant energy scale determining the stability of the system is provided by the concentration and arrangement of the HS Co^{3+} ions with an energy scale of 100 meV/cell, as shown in Fig. 3 (a). Therefore, our strategy is that we first consider FM-ordered HS/LS states to study the overall stability and behavior of the HS/LS configurations under epitaxial strain. In section 5, we will explore the exchange interaction in the HS/LS state with the most stable geometrical configuration under tensile strain.

The first important finding is that when LCO forms HS Co^{3+} ions, it is energetically favorable to separate them by LS Co^{3+} rather than having them to be the first nearest neighbors. Furthermore, we find that tensile-strained LCO becomes more stable as the number of these second nearest neighbor HS pairs increases as shown in Fig. 3 (a). Overall we find that a 1:1 HS/LS mixed configuration (c5 in Fig. 3 (a)) is the most stable magnetic solution for LCO under 3.5% strain. The total energy of this configuration is 54 meV/formula-unit below that of NM LCO. In Fig. 3 (b), we show the 3*d*-projected density of states at the LS and upper HS Co^{3+} sites along the *c*-axis direction for the 1:1 HS/LS state. There is an energy gap of 0.5 eV at the Fermi level defined by the t_{2g}* and e_g* splitting of the LS Co^{3+} sites. For the HS Co^{3+} site, the on-site *U* and *J* produce localized states from -8.0 to -5.0 eV in the spin-up channel, and empty d_{xz} and

d_{yz} states in the spin down channel, consistent with the mean field picture of the HS state. The presence of the energy gap in the HS/LS mixed state is consistent with strained LCO being insulating [7].

To elucidate the effect of epitaxial strain on the magnetic state of LCO, we compare in Fig. 4 the energy as a function of strain for mixed HS/LS configurations with 25% and 50% concentration of HS Co^{3+}, the homogeneous IS state (previously considered in Ref. [10]), and NM LCO for reference. We see that the HS/LS mixed states are stable when compared to the homogeneous IS state at all strain levels, and that above a tensile strain of 2.5%, the HS/LS states become more stable than NM LCO. Under zero strain, there is an energy cost to excite LS Co^{3+} to HS Co^{3+}. Comparing the energy of a dilute HS/LS configuration with a HS Co^{3+} concentration of 12.5% to that of NM LCO, we estimate the energy cost of the excitation to be 62 meV/Co^{3+}. However, as a function of tensile strain, the energy of the mixed HS/LS states (see Fig. 3) increases more slowly than that of NM LCO, inducing a spin state transition at 2.5%. It is also evident from Fig. 4 that LCO with higher concentration of HS Co^{3+} is softer against tensile strain [6], and that compressive strain doesn't stabilize a magnetic state [6,7,12].

IV. Electronic and Structural Response of $LaCoO_3$ under Epitaxial Strain

To shed more light on the mechanism of the strain-induced spin state transition in LCO, we plot the energy gap in NM LCO as a function of strain in Fig. 5 (a). The energy gap in LCO forms between the t_{2g}* and e_g* bands and is given by $10Dq - [W(e_g^*) + W(t_{2g}^*)]/2$, where $10Dq$ is the crystal field splitting and W's are the bandwidths of corresponding bands. Under epitaxial strain, the local symmetry at the Co^{3+} site is lowered from cubic (O_h) to tetragonal (D_{4h}) and the degeneracy in the t_{2g}* and e_g* manifolds is lifted as shown in Fig. 5 (b). Furthermore, the change in the Co-O bond length and the Co-O-Co bond angle modifies the bandwidths [46]. In Fig. 5 (a), we see that the energy gap becomes less than 58 meV above a strain level of 2.5%, thus allowing for the spin state transition [22]. Note, however, that the band gap also narrows for compressively strained LCO, but this does not result in a magnetic solution as shown in Fig. 4. Our result suggests that the standard picture in terms of the competition between the crystal field splitting and the Hund's rule coupling is not sufficient to consistently describe magnetism in strained LCO. Instead, we find that there is an important structural transition in LCO under tensile strain that accompanies the spin state transition.

When biaxially strained, LCO responds in the out-of-plane c direction due to the Poisson effect [6,10] (see Fig. 2). Since the LS CoO_6 unit is rigid due to covalency of the Co-O bond (bond stretching costs a large amount of energy), strain is mainly accommodated by tilting and rotation of CoO_6 octahedra [47]. Microscopically, this is achieved by changes in the Co-O-Co angles (θ_{in} and θ_{out} in Fig. 1 (a)) accompanied by slight changes in the Co-O bond length (b_{in} and b_{out} in Fig 1 (a)) or local tetragonality ($\Delta_{TD} = 2\times(b_{in}-b_{out})/|b_{in}+b_{out}|$). As shown in Fig. 6 (a), in NM LCO, local tetragonality increases almost linearly as tensile or compressive strain is applied. In a simple model, the energy curve for NM LCO in Fig. 4, could be thought of as $\frac{1}{2}k\Delta_{TD}^2$, where k is a spring constant determined by the covalent mixing between Co 3d and O 2p states. Therefore, to minimize the bond stretching or Δ_{TD} under tensile strain, the octahedral rotation is largely suppressed (θ_{in} greater than the bulk value) while the tilting is enhanced (θ_{out} smaller than the bulk value) as shown in Fig. 6 (c) and (d). The opposite is true for compressive strain: θ_{in} becomes smaller than the bulk value in conjunction with the disappearance of the tilting mode (θ_{out} =180°).

Interestingly, we find that strained 1:1 HS/LS LCO undergoes an unusual structural transition above 1.5% tensile strain. It manifests as a substantial increase in Δ_{TD} of the HS CoO_6 clusters as shown in Fig. 6 (a) and (b). On the other hand, Δ_{TD} of the LS clusters in 1:1 HS/LS LCO drops by more than a factor of two compared to NM LCO. This suggests that above 1.5%, tensile strain is accommodated mainly by the HS CoO_6 units through bond length changes, allowing the LS octahedra to be less distorted thus relieving their elastic energy. This is possible because HS Co^{3+} has a softer Co-O bond under stretch [48-50]. As a result, both bond angles θ_{in} and θ_{out} almost recover their bulk values since octahedral rotation and tilting are no longer needed for strain accommodation (Fig. 6 (c) and (d)).

One way to rationalize this effect is to assume that at the spin state transition under tensile strain, the spring constant between HS Co^{3+} and O becomes *k′,* which is significantly less than *k* of LS CoO_6 units. This is evident from the electronic structure shown in Fig. 3 (b). The strong on-site interactions *U* and *J* produce localized orbitals for the HS configuration while sacrificing the hybridization between Co 3*d* and O 2*p*. In Fig. 3 (c), we show the valence charge distribution in the CoO_2 plane for the 1:1 HS/LS mixed state. Note that less charge is accumulated along the HS Co-O bonds due to reduced hybridization when compared to that of the LS Co-O bonds [14]. Therefore, although replacing LS Co^{3+} ions with HS ones costs energy (≈62 meV/Co^{3+}), the relative softness of HS CoO_6 clusters pays off beyond 2.5% strain. On the contrary, this type of structural transition does not occur under compressive strain as shown in Fig. 4 (a). If it were to occur, the HS CoO_6 units would further contract in the *ab* plane, which is incompatible with the known tendency of HS Co^{3+} to occupy a larger local volume [20,51].

V. Superexchange Interaction in the 1:1 HS/LS Mixed State.

We note that the magnetic moments in the mixed 1:1 HS/LS configuration of 3.5% tensile-strained LCO are well localized at the HS Co^{3+} sites. Therefore, to map the exchange coupling between the local moments, we use an effective Heisenberg Hamiltonian for the exchange energy of the system [29,30]:

$$H = -\sum_{i \neq j} J^{ij} \vec{e}_i \cdot \vec{e}_j , \quad (1)$$

where $\vec{e}_{i(j)}$ is the local moment at site *i(j)* and J^{ij} are the exchange parameters. We consider five different collinear magnetic configurations as shown in Fig. 7 to calculate the parameters for the first (coordination number = 12) and the second nearest neighbor (n.n.) (coordination number = 6) interactions. We note that the in-plane exchange constant *J* is different from the out-of-plane *J* owing to the tetragonal distortion in strained LCO on STO. This yields four coupling constants $J_{1,in}$, $J_{1,out}$, $J_{2,in}$, and $J_{2,out}$. To calculate $J_{1,in}$ and $J_{1,out}$, we use the 2×2×2 cell (see Fig. 7 (a)), while we double the cell along the *a*-axis (the *c*-axis) to calculate $J_{2,\,in}$ ($J_{2,\,out}$) (see Fig. 7 (b)). We further emphasize that both J_1*'s* and J_2*'s* are important to consider on the same footing since two adjacent HS Co^{3+} interact *via* superexhcange mechanism [53,54], involving virtual hopping of e_g electrons and t_{2g} holes from HS Co^{3+} sites to the n.n. LS Co^{3+} site. As shown in Fig. 7, both the first and second n.n. HS Co^{3+} pairs are separated by one LS Co^{3+} ion but with different angles: 90° (180°) for the first (second) n.n HS Co^{3+} pair. This means that the interaction strength is of the same order of magnitude in both cases. In Table 2, we list the exchange energies of the magnetic configurations in Fig. 7 along with the calculated exchange parameters. We find that the first n.n. coupling $J_{1,in}$ and $J_{1,out}$ are ferromagnetic and 2.5 and 2.7 meV/pair, respectively [55]. However, we

observe that the second n.n. couplings are strongly antiferromagnetic and $|J_{2,out}|$ is larger than $|J_1|$'s by more than a factor of two.

To better understand the qualitative features of the exchange parameters, we consider an effective e_g model where the relatively small hopping matrix elements between t_{2g} electrons are not included [56]. In Fig. 8 (a), we show the configuration of the 1:1 HS/LS state in the *ac* plane. The key difference between the first and second n.n. interactions originates from the hopping matrices. The first n.n. coupling involves both the out-of-plane and in-plane hopping matrices, which are described by $\boldsymbol{t_c}$ and $\boldsymbol{t_a}$, respectively. Considering the orbital symmetry, $\boldsymbol{t_c}$ and $\boldsymbol{t_a}$ can be written as,

$$\boldsymbol{t_c} = t\begin{pmatrix} 1 & 0 \\ 0 & 0 \end{pmatrix} \text{ and } \boldsymbol{t_a} = \frac{t'}{4}\begin{pmatrix} 1 & -\sqrt{3} \\ -\sqrt{3} & 3 \end{pmatrix}, \text{ respectively,} \tag{2}$$

where we use $\{|d_{3z^2-r^2}\rangle, |d_{x^2-y^2}\rangle\}$ as a basis and *t(t')* is the effective *d-d* hopping constant [56]. For the out-of-plane hopping matrix $\boldsymbol{t_c}$, we only consider the dominant hopping t between $|d_{3z^2-r^2}\rangle$ states, for simplicity. Once we fix the hopping matrix along the *c*-axis, the in-plane hopping matrix $\boldsymbol{t_a}$ can be obtained by a coordinate transformation. Note, however, that the in-plane hopping parameter t' should be smaller than the out-of-plane t due to the tetragonal distortion in tensile-strained LCO. Using the full e_g bandwidth W of approximately 4.0 eV in bulk LCO, we estimate the effective *d-d* hopping for unstrained LCO to be about 0.7 eV ($\approx W/6$) [56]. For 3.5% tensile-strained LCO, we have shown that the bond angles are close to the bulk values, therefore the change in the hopping constant under tensile strain mainly arises from the bond length changes. Using our structural data along with Harrison's formula ($t_{dd} \sim 1/d^5$, where d is the inter-atomic distance)[52],we calculate $t \approx 0.8$ eV and $t' \approx 0.6$ eV.

We first consider the superexchange path for the first n.n. HS–LS–HS cluster. Table 3 shows the relevant states for the superexchange interaction in terms of the e_g occupancy at the HS or LS sites. The state S1 is the insulating FM- or AFM-ordered ground state of the 1:1 HS/LS state in the absence of hopping. The states S2, S3, and S4 are virtual excited states that can be reached by one electron hopping from S1. For S2 and S3, we introduce the energy cost Δ for transferring one electron from the HS site to the LS site. In principle, Δ can be determined self-consistently, but we treat it as an empirical parameter in this qualitative calculation. The most important state for the superexchange interaction is S4, whose energy is determined by the on-site repulsion U and Hund's coupling J_H. For instance, state S4 which is derived from FM-ordered S1 is shown in Fig. 8 (b). Considering the hopping matrices $\boldsymbol{t_a}$ and $\boldsymbol{t_c}$, we construct the Hamiltonian for the FM- and AFM-ordered states as follows:

$$H_{\uparrow\uparrow(\uparrow\downarrow)} = \begin{pmatrix} 0 & t & t'/4 & -\sqrt{3}t'/4 & -\sqrt{3}t'/4 & 3t'/4 & 0 & 0 \\ t & \Delta & 0 & 0 & 0 & 0 & -\sqrt{3}t'/4 & 3t'/4 \\ t'/4 & 0 & \Delta & 0 & 0 & 0 & 0 & 0 \\ -\sqrt{3}t'/4 & 0 & 0 & \Delta & 0 & 0 & t & 0 \\ -\sqrt{3}t'/4 & 0 & 0 & 0 & \Delta & 0 & 0 & 0 \\ 3t'/4 & 0 & 0 & 0 & 0 & \Delta & 0 & t \\ 0 & -\sqrt{3}t'/4 & 0 & t & 0 & 0 & 2\Delta + U - (+)J_H & 0 \\ 0 & 3t'/4 & 0 & 0 & 0 & t & 0 & 2\Delta + U - (+)J_H \end{pmatrix}, \tag{3}$$

where we use t≈0.8 eV, t'≈0.6 eV, U≈5.0 eV, J_H≈1.5 eV, and Δ≈2 eV. The exchange parameter $J_{1,out}$ is then calculated as:

$$-2J_{1,out} = E(FM) - E(AFM), \tag{4}$$

where *E(FM/AFM)* is the energy gain for the FM/AFM-ordered state due to superexchange.

On the other hand, the superexchange interaction of the second n.n. HS-LS-HS cluster in the *ac*-plane only involves the hopping matrix $\boldsymbol{t_c}$ (see Fig. 8 (a)). Therefore, the Hamiltonian for the FM-ordered state only involves configurations S1, S2, and S3 in Table 3, while S4 can contribute to the exchange energy gain for the AFM-ordered state (see Fig 8 (b)). The Hamiltonian matrices are written as:

$$H_{\uparrow\uparrow} = \begin{pmatrix} 0 & t & t \\ t & \Delta & 0 \\ t & 0 & \Delta \end{pmatrix}, \tag{5}$$

and

$$H_{\uparrow\downarrow} = \begin{pmatrix} 0 & t & t & 0 \\ t & \Delta & 0 & t \\ t & 0 & \Delta & t \\ 0 & t & t & 2\Delta + U' + J_H \end{pmatrix}, \tag{6}$$

where U' is the intra-orbital repulsion, for which we use $U'=U+2J_H$ [16]. Including the *ab*-plane exchange interactions, we calculate the exchange parameters as 1.9, 1.2, -7.9, and -3.1 eV for $J_{1,out}$, $J_{1,in}$, $J_{2,out}$, and $J_{2,in}$, respectively. These results are in qualitative agreement with the DFT results shown in Table 2. Therefore, we show that the larger second n.n. AFM coupling parameters originate from the difference between the hopping matrices involved for J_1 and J_2.

VI. Non-collinear magnetic structure in tensile-strained $LaCoO_3$

To explore the effect of $J_{2,out}$ in the 1:1 HS/LS configuration of tensile-strained (3.5%) LCO, we perform several calculations based on the unconstrained non-collinear spin density functional formalism [57]. The spin-orbit coupling is ignored. In these calculations, only the relative angles between the local moments determine the exchange energy. The calculations are done using the $\sqrt{2}\times\sqrt{2}\times4$ cell that has 8 independent Co sites. First, we introduce a polar angle θ for half of the local moments as shown in Fig. 9 (a) and calculate the energy of the system as a function of the angle. The magnetic structure with angle θ of zero and 180° corresponds to the collinear FM and AFM3 configurations in Fig. 7, respectively. As shown in Fig. 9 (a), the fully FM-ordered state is unstable in the presence of the strong second n.n. antiferromagnetic coupling and, as a result, we find that the most stable collinear structure is AFM3 (net magnetization = 0). We find that this is also the case for LCO under different tensile strain levels. However, we point out that the energy difference between the FM and AFM3 structure is small (~2.3 meV/Co^{3+}).

To search for possible low energy canted spin structures in tensile-strained LCO, we introduce an additional azimuthal angle φ for the local moment as shown in Fig. 9 (b). Considering a large set of different θ and φ for each local moment, we find multiple solutions that are degenerate with AFM3. One

of the lowest energy canted spin structures is shown in Fig. 9 (b). The spin moments rotate by 90 degrees (for φ) as it goes to the next upper *ab*-plane according to the second n.n. AFM coupling. However, half of the local moments are slightly canted toward the *c*-axis, yielding a small magnetic moment of about 0.26 μ_B/Co^{3+} in the system [10]. Our results suggest that the relatively low magnetic moment of 0.7 μ_B/Co^{3+} in experiment [10] may be due to the presence of the strong AFM coupling screening the FM ordering in the system. Finally, we remark that this particular type of canted structure considered in Fig. 9 (b) may not be the lowest energy structure even in theory, since we are still limited by the size of the cell. Furthermore, noting that in a typical magnetic measurement a small magnetic field is applied at finite temperature, another canted ferromagnetic state may be stabilized.

VII. Summary

In conclusion, we explain the mechanism of strain-induced spin state transition and examine the exchange interaction in tensile-strained $LaCoO_3$. Considering various high-spin/low-spin configurations, we show that high-spin Co^{3+} ions in LCO prefer to be separated by low-spin Co^{3+} ions. We further demonstrate that above a tensile strain of 2.5%, the ground state of LCO is an insulator with a 1:1 HS/LS mixed state. In contrast, compressive strain is not able to produce a magnetic state. We attribute the stabilization of the HS/LS state to increased compliance of LCO when it has a higher concentration of HS Co^{3+} ions. We examine the exchange parameters in the 1:1 HS/LS state of tensile-strained LCO by considering various collinear magnetic structures. The first nearest neighboring couplings are ferromagnetic with strength of 2.5 and 2.7 meV/pair in the in-plane and out-of-plane directions, respectively. However, the second nearest neighbor couplings are strongly antiferromagnetic with strengths of -3.3 and -7.7 meV/pair in the in-plane and out-of-plane directions, respectively. Due to the strong antiferromagnetic coupling, we find that the lowest energy collinear structure is one with an up-up-down-down order along the *c*-direction. However, we show that the competition between the FM and AFM couplings in the system may lead to a canted (non-collinear) spin structure with a finite net magnetization.

Acknowledgement
We thank Chungwei Lin for helpful discussions. This work is supported by the National Science Foundation under grant DMR-0548182, the US Department of Energy (DOE) under grant DE-SC0001878, and Texas Advanced Computing Center.

REFERENCES

[1] A.Ohtomo, D. A. Muller, J. L. Grazul and H. Y. Hwang, *Nature* **419**, 378 (2002).
[2] J. H. Lee, L. Fang, E. Vlahos, X. Ke, Y. W. Jung, L. F. Kourkoutis, J.-W. Kim, P. J. Ryan, T. Heeg, M. Roeckerath, V. Goian, M. Bernhagen, R. Uecker, P. C. Hammel, K. M. Rabe, S. Kamba, J. Schubert, J. W. Freeland, D. A. Muller, C. J. Fennie, P. Schiffer, V. Gopalan, E. Johnston-Halperin and D. G. Schlom, *Nature* **466**, 954 (2010).
[3] R. J. Zeches, M. D. Rossell, J. X. Zhang, A. J. Hatt, Q. He, C.-H. Yang, A. Kumar, C. H. Wang, A. Melville, C. Adamo, G. Sheng, Y.-H. Chu, J. F. Ihlefeld, R. Erni, C. Ederer, V. Gopalan, L. Q. Chen, D. G. Schlom, N. A. Spaldin, L. W. Martin, and R. Ramesh, *Science* **326**, 977 (2009).

[4] J. Chakhalian, J. M. Rondinelli, Jian Liu, B. A. Gray, M. Kareev, E. J. Moon, N. Prasai, J. L. Cohn, M. Varela, I. C. Tung, M. J. Bedzyk, S. G. Altendorf, F. Strigari, B. Dabrowski, L. H. Tjeng, P. J. Ryan, and J. W. Freeland, *Phys. Rev. Lett.* **107**, 116805 (2011).
[5] D. Fuchs, C. Pinta, T. Schwarz, P. Schweiss, P. Nagel, S. Schuppler, R. Schneider, M. Merz, G. Roth, and H. v. Löhneysen, *Phys. Rev. B* **75**, 144402 (2007).
[6] D. Fuchs, E. Arac, C. Pinta, S. Schuppler, R. Schneider, and H. b. Löhneysen, *Phys. Rev. B* **77**, 014434 (2008).
[7] J. W. Freeland, J. X. Ma, and J. Shi, *Appl. Phys. Lett.* **93**, 212501 (2008).
[8] A. Herklotz, A. D. Rata, L. Schultz, and K. Dörr, *Phys. Rev. B* **79**, 092409 (2009).
[9] S. Park, P. Ryan, E. Karapetrova, J. W. Kim, J. X. Ma, J. Shi, J. W. Freeland, and W. Wu, *Appl. Phys. Lett.* **95**, 072508 (2009).
[10] A. Posadas, M. Berg, H. Seo, A. de Lozanne, A. A. Demkov, D. J. Smith, A. P. Kirk, D. Zhernokletov, and R. M. Wallace, *Appl. Phys. Lett.* **98**, 053104 (2011).
[11] V. Mehta, M. Liberati, F. J. Wong, R. V. Chopdekar, E. Arenholz, and Y. Suzuki, *J. Appl. Phys.* **105**, 07E503 (2009).
[12] V. Mehta and Y. Suzuki, *J. Appl. Phys.* **109**, 07D717 (2011).
[13] M. Merz, P. Nagel, C. Pinta, A. Samartsev, H. v. Löhneysen, M. Wissinger, S. Uebe, A. Assmann, D. Fuchs, and S. Schuppler, *Phys. Rev. B* **82**, 174416 (2010).
[14] G. E. Sterbinsky, P. J. Ryan, J.-W. Kim, E. Karapetrova, J. X. Ma, J. Shi, and J. C. Woicik, *Phys. Rev. B* **85**, 020403(R) (2012).
[15] M. A. Senaris-Rodriguez and J. B. Goodenough, *J. of Solid State Chemistry* **116**, 224 (1995).
[16] S. Maekawa, T. Tohyama, S. E. Barnes, S. Ishihara, W. Koshibae, G. Khaliullin, *Physics of transition metal oxides* (Springer-Verlag, Berlin, 2004).
[17] P. M. Raccah and J. B. Goodenough, *Phys. Rev.* **155**, 932 (1967).
[18] A. Podlesnyak, S. Streule, J. Mesot, M. Medarde, E. Pomjakushina, K. Conder, A. Tanaka, M. W. Haverkort, and D. I. Khomskii, *Phys. Rev. Lett.* **97**, 247208 (2006).
[19] M. A. Korotin, S. Yu. Ezhov, I. V. Solovyev, V. I. Anisimov, D. I. Khomskii and G. A. Sawatzky, *Phys. Rev. B* **54**, 5309 (1996).
[20] P. G. Radaelli and S. W. Cheong, *Phys. Rev. B* **66**, 094408 (2002).
[21] M. Zhuang, W. Zhang, and N. Ming, *Phys. Rev. B.* **57**, 10705 (1998).
[22] M. W. Haverkort, Z. Hu, J. C. Cezar, T. Burnus, H. Hartmann, M. Reuther, C. Zobel, T. Lorenz, A. Tanaka, N. B. Brookes, H. H. Hsieh, H.-J. Lin, C. T. Chen, and L. H. Tjeng, *Phys. Rev. Lett.* **97**, 176405 (2006).
[23] K. Knížek, Z. Jirák, J. Hejtmánek, P. Novák, and W. Ku, *Phys. Rev. B* **79**, 014430 (2009).
[24] J. Kuneš and V. Křápek, *Phys. Rev. Lett.* **106**, 256401 (2011).
[25] H. Hsu, P. Blaha, R. M. Wentzcovitch, and C. Leighton, *Phys. Rev. B* **82**, 100406(R) (2010).
[26] K. Gupta and P. Mahadevan, *Phys. Rev. B* **79**, 020406 (2009).
[27] J.M. Rondinelli and N.A. Spaldin, *Phys. Rev. B* **79**, 054409 (2009).
[28] H. Hsu, P. Blaha, and R. M. Wentzcovitch, *Phys. Rev. B* **85**, 140404(R) (2012).
[29] J. Lee and A. A. Demkov, *Phys. Rev. B* **82**, 235305 (2010).
[30] G. Fischer, M. Däne, A. Ernst, P. Bruno, M. Lüders, Z. Szotek, W. Temmerman, and W. Hergert, *Phys. Rev. B* **80**, 014408 (2009).
[31] G. Kresse and J. Furthmüller, *Phys. Rev. B* **54**, 11169 (1996).
[32] P. E. Blöchl, *Phys. Rev. B* **50**, 17953 (1994); G. Kresse and D. Joubert, *Phys. Rev. B* **59**, 1758 (1999).

[33] S.L. Dudarev, G.A. Botton, S.Y. Savrasov, C.J. Humphreys, and A.P. Sutton, *Phys. Rev. B* **57**, 1505 (1998).
[34] A. I. Liechtenstein, V. I. Anisimov, J. Zaanen, *Phys. Rev. B* **52**, R5467 (1995).
[35] J. P. Perdew and A. Zunger, *Phys. Rev. B* **23**, 5048 (1981).
[36] F. M. de Groot, J. C. Fuggle, B. T. Thole, and G. A. Sawatzky, *Phys. Rev. B* **42**, 5459 (1990).
[37] M. Abbate, J. C. Fuggle, A. Fujimori, R. Potze, G. A. Sawatzky, H. Eisaki, and S. Uchida, *Phys. Rev. B* **47**, 16124 (1993).
[38] M. Abbate, R. Potze, G. A. Sawatzky, and A. Fujimori, *Phys. Rev. B* **49**, 7210 (1994).
[39] T. Saitoh, T. Mizokawa, A. Fujimori, M. Abbate, Y. Takeda, and M. Takano, *Phys. Rev. B* **55**, 4257 (1997).
[40] A. Chainani, M. Mathew, and D. D. Sarma, *Phys. Rev. B* **46**, 9976 (1992).
[41] P. G. Radaelli and S. W. Cheong, *Phys. Rev. B* **66**, 094408 (2002).
[42] A. M. Glazer, *Acta Cryst. B* **28**, 3384 (1972).
[43] P. M. Woodward, *Acta Cryst.* B **53**, 32 (1997), P. M. Woodward, *Acta Cryst.* B **53**, 44 (1997).
[44] H. J. Monkhorst and J. D. Pack. *Phys. Rev. B* **13**, 5188 (1976).
[45] J. B. Goodenough, *Phys. Rev.* **100**, 564 (1955); J. B. Goodenough, *J. Phys. Chem. Solids* **6**, 287 (1958); J. Kanamori, *J. Phys. Chem. Solids* **10**, 87 (1959); P. W. Anderson, *Solid State Phys.* **14**, 99 (1963).
[46] J. –S. Zhou, J. –Q. Yan, and J. B. Goodenough, *Phys. Rev. B* **71**, 220103(R) (2005).
[47] S. J. May, J.-W. Kim, J. M. Rondinelli, E. Karapetrova, N. A. Spaldin, A. Bhattacharya, and P. J. Ryan, *Phys. Rev. B* **82**, 014110 (2010).
[48] T. Vogt, J. A. Hriljac, N.C. Hyatt, and P. Woodward, *Phys. Rev. B* **67**, 140401(R) (2003).
[49] J. –S. Zhou, J. –Q. Yan, and J. B. Goodenough, *Phys. Rev. B* **71**, 220103 (R) (2005).
[50] The bulk modulus of LCO with 0%, 25%, 50% and 100% concentrations of HS Co^{3+} is calculated to be 203, 186, 181, and 176 GPa, respectively, showing significant softening as concentration of HS Co^{3+} increases.
[51] The ionic radius of HS Co^{3+} is calculated to be larger than that of LS Co^{3+} by 0.05 Å, which is in good agreement with the experimental values of r_{LS} = 0.545 Å and r_{HS} = 0.61 Å.
[52] W. A. Harrison, *Electronic Structure and the Properties of Solids* (Dover, Mineola, N.Y., 1989).
[53] A. J. Millis, *Phys. Rev. B* **55**, 6405 (1997).
[54] D. I. Khomskii and G. A. Sawatzky, *Solid State Comm.* **102**, 87 (1997).
[55] To ensure that the FM coupling is robust in a reasonable range of U_{eff}, we test three U_{eff} values of 3.0, 3.5, and 4.0 eV, yielding coupling strengths of 3.0, 2.8 and 2.6 meV/pair, respectively.
[56] C. Ederer, C. Lin, and A. J. Millis, *Phys. Rev. B* ***76***, 155105 (2007).
[57] D. Hobbs, G. Kresse, and J. Hafner, *Phys. Rev. B* **62**, 11556 (2000).

TABLES

Table 1. Ground state structure ($R\bar{3}c$) of non-magnetic insulating $LaCoO_3$

	a (Å)	α (°)	x	Co-O length (Å)	Co-O-Co angle (°)
Theory (this work)	5.249	61.13	0.5528	1.893	162.87
Experiment[a] (T=5K)	5.345	61.01	0.5527	1.925	162.93

[a] Reference 20.

Table 2. Exchange energy gain for several magnetic configurations[a] and exchange parameters of the 1:1 HS/LS state of 3.5% tensile-strained $LaCoO_3$

Configuration[a]	Energy (meV/cell)	Exchange parameter	(meV/pair)
FM	$-8J_{1,in} - 16J_{1,out} - 8J_{2,in} - 4J_{2,out}$	$J_{1,out}$	2.7
AFM1	$-8J_{1,in} + 16J_{1,out} - 8J_{2,in} - 4J_{2,out}$	$J_{1,in}$	2.5
AFM2	$8J_{1,in} - 8J_{2,in} - 4J_{2,out}$	$J_{2,out}$	-7.7
AFM3	$-16J_{1,in} - 16J_{2,in} + 8J_{2,out}$	$J_{2,in}$	-3.3
AFM4	$-16J_{1,out} - 8J_{2,out}$		

[a] The collinear magnetic configurations are shown in Fig. 7.

Table 3. States distinguished by occupancy at the HS and LS Co^{3+} sites and their energies

State	HS Co^{3+}	LS Co^{3+}	HS Co^{3+}	Energy
S1	2	0	2	0
S2	1	1	2	Δ
S3	2	1	1	Δ
S4	1	2	1	$2\Delta+U-J_H$ (↑↑)
				$2\Delta+U+J_H$ (↑↓)

FIGURE CAPTIONS

FIG. 1. (Color online) (a) Rhombohedral unit cell of $LaCoO_3$ with the large sphere representing La, the medium-sized sphere representing Co, and the small sphere representing O. (b) $\sqrt{2}\times\sqrt{2}\times 2$ tetragonal supercell of $LaCoO_3$. b_{in} (b_{out}) stands for in-plane (out-of-plane) Co-O bond length. θ_{in} (θ_{out}) stands for in-plane (out-of-plane) Co-O-Co bond angle.

FIG. 2. (Color online) Optimized *c* lattice constant (a) and cell volume (b) of LCO with different magnetic states. NM means non-magnetic LCO, HS/LS (1:3) or (1:1) mean ferromagnetic LCO with a HS/LS mixed spin state with the ratio of 1:3 or 1:1.

FIG. 3. (Color online) (a) Energy of LCO with HS/LS mixed spin states per 2×2×2 cell (eight formula units) under a tensile strain of 3.5%. Energy of NM LCO is set to 0 eV. Insets are schematic pictures of the geometrical arrangement of HS Co^{3+} ions for each HS/LS configuration (c1 to c5). Dark spheres indicate Co^{3+} sites with La and O sites omitted for clarity. White arrows in the large spheres represent spins at the HS Co^{3+} sites. (b) Projected density of states for 3*d* orbitals in the 1:1 HS/LS mixed state (c5 in Fig. 3 (a)) at LS Co^{3+} site (upper panel) and out-of-plane HS Co^{3+} site (lower panel). The Fermi energy (dashed vertical line) is set to 0 eV. Positive (negative) DOS is for spin-up (spin-down). (c) Cross-sectional valence charge distribution of the 1:1 HS/LS mixed state at the CoO_2 plane with contours overlaid. The contours are drawn for the charge density from 0.5 to 1.0 eÅ^{-3} usiang a step interval of 0.04 eÅ^{-3} to contrast the charge accumulations at the HS Co-O bonds (dotted arrows) with the LS Co-O bonds (solid arrows).

FIG. 4. (Color online) Energy of LCO per $\sqrt{2}\times\sqrt{2}\times 2$ cell (four formula units) as a function of strain for non-magnetic (filled squares), homogeneous IS (up triangles), 1:3 HS/LS (down triangles), and 1:1 HS/LS states (right triangles).

FIG. 5. (Color online) (a) Energy gap between the t_{2g}* and e_g* bands of nonmagnetic LCO as a function of strain. (b) Energy level splitting of LS Co^{3+} under compressive or tensile strain

FIG. 6. (Color online) (a) Local tetragonality ($\Delta_{TD} = 2\times(b_{in}-b_{out})/|b_{in}+b_{out}|$) as a function of strain for CoO_6 octahedra in NM LCO (squares), for HS Co^{3+} sites (down triangles) and LS Co^{3+} sites (up triangles) in 1:1 HS/LS FM LCO. (b) Schematic of octahedral distortion in 1:1 HS/LS FM LCO above 1.5% strain. Lateral arrows stand for the epitaxial constraint in the *ab* plane imposed by biaxial tensile strain while vertical arrows stand for the contraction of LCO in the *c*-direction due to the Poisson effect. In-plane (c) and out-of-plane (d) Co-O-Co angles as a function of strain for NM LCO (squares) and 1:1 HS/LS FM LCO (triangles). θ_0 is the theoretical Co-O-Co angle in the LCO bulk.

FIG. 7. (Color online) Schematic pictures of collinear magnetic structures of HS/LS mixed states. To calculate the first n.n. coupling parameters ($J_{1,out}$ and $J_{1,in}$), the 2×2×2 supercell is used (a) and the 2×2×4 (left) or 4×2×2 (right) supercell is used for the second n.n. coupling parameters ($J_{2,out}$ and $J_{2,in}$) (b). Subscripts 'out' and 'in' for the coupling parameters stand for out-of-plane and in-plane, respectively.

Dark spheres indicate Co^{3+} sites with La and O sites omitted for clarity. White and black arrows in the large spheres represent spins at the HS Co^{3+} sites.

FIG. 8. (Color online) (a) Schematic of the superexchange paths for the first (J_1) and second (J_2) n.n. couplings of the 1:1: HS/LS mixed state in the *ac*-plane. Only the e_g levels ($|d_{3z^2-r^2}\rangle, |d_{x^2-y^2}\rangle$) are shown. Diagrams illustrating the ferromagnetic (b) and antiferromagnetic (c) superexchange interactions for the first and the second n.n. couplings in the 1:1 HS/LS state, respectively. See the main text for the model description.

FIG. 9. (Color online) (a) Energy of tensile-strained LCO with the 1:1 HS/LS configuration as a function of canting angle θ. Inset shows a canted spin configuration with angle θ in the *ac*-plane. Black arrows represent the local moments at the HS Co^{3+} sites. The $\sqrt{2}\times\sqrt{2}\times4$ calculation cell used has eight formula units. (b) Schematic of a local moment described by polar angle θ and azimuthal angle φ (left). This arrangement is one of the lowest energy canted spin structures of tensile-strained LCO (right). La atoms and other small magnetic moments at LS Co^{3+} and O sites are omitted for clarity.

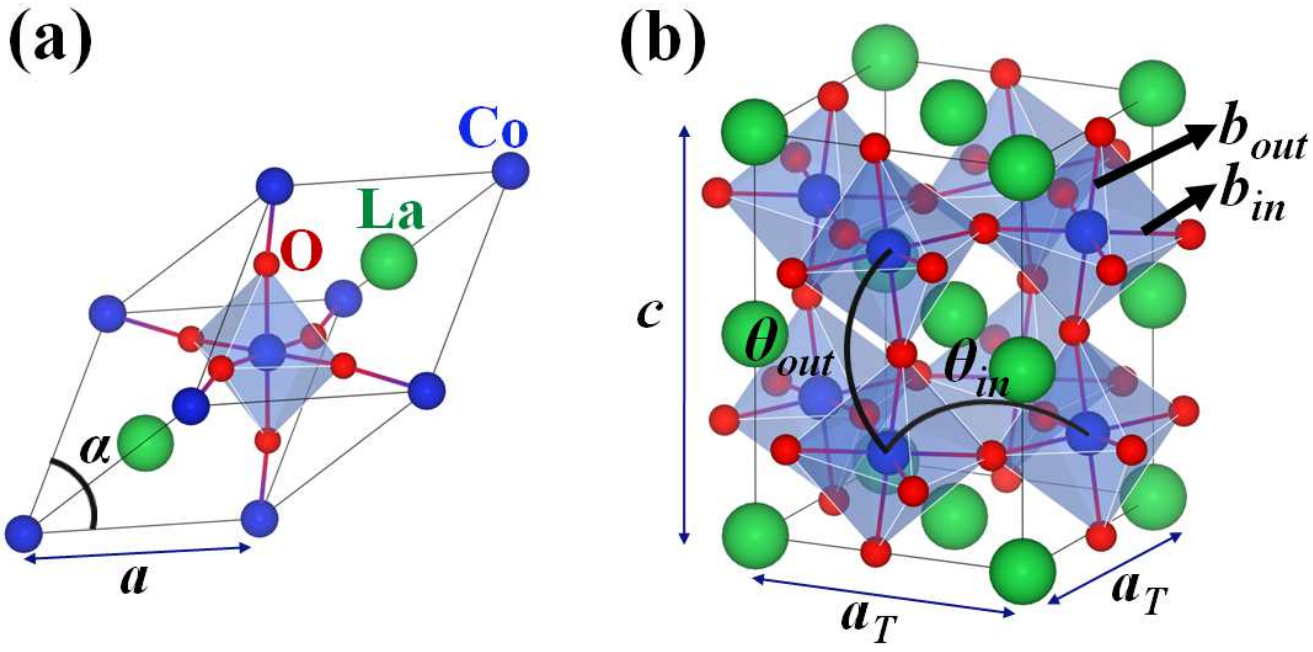

Figure 1 LK12746B 10JUL2012

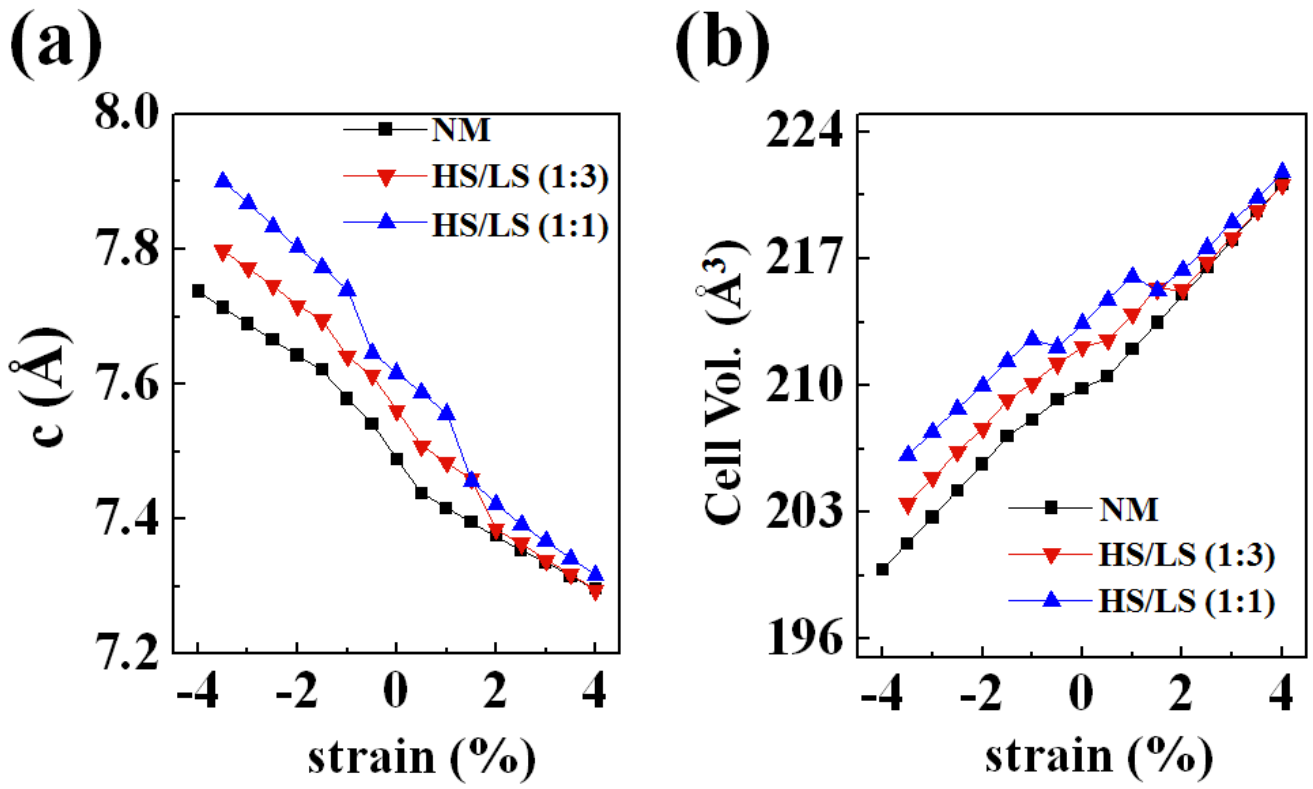

Figure 2 LK12746B 10JUL2012

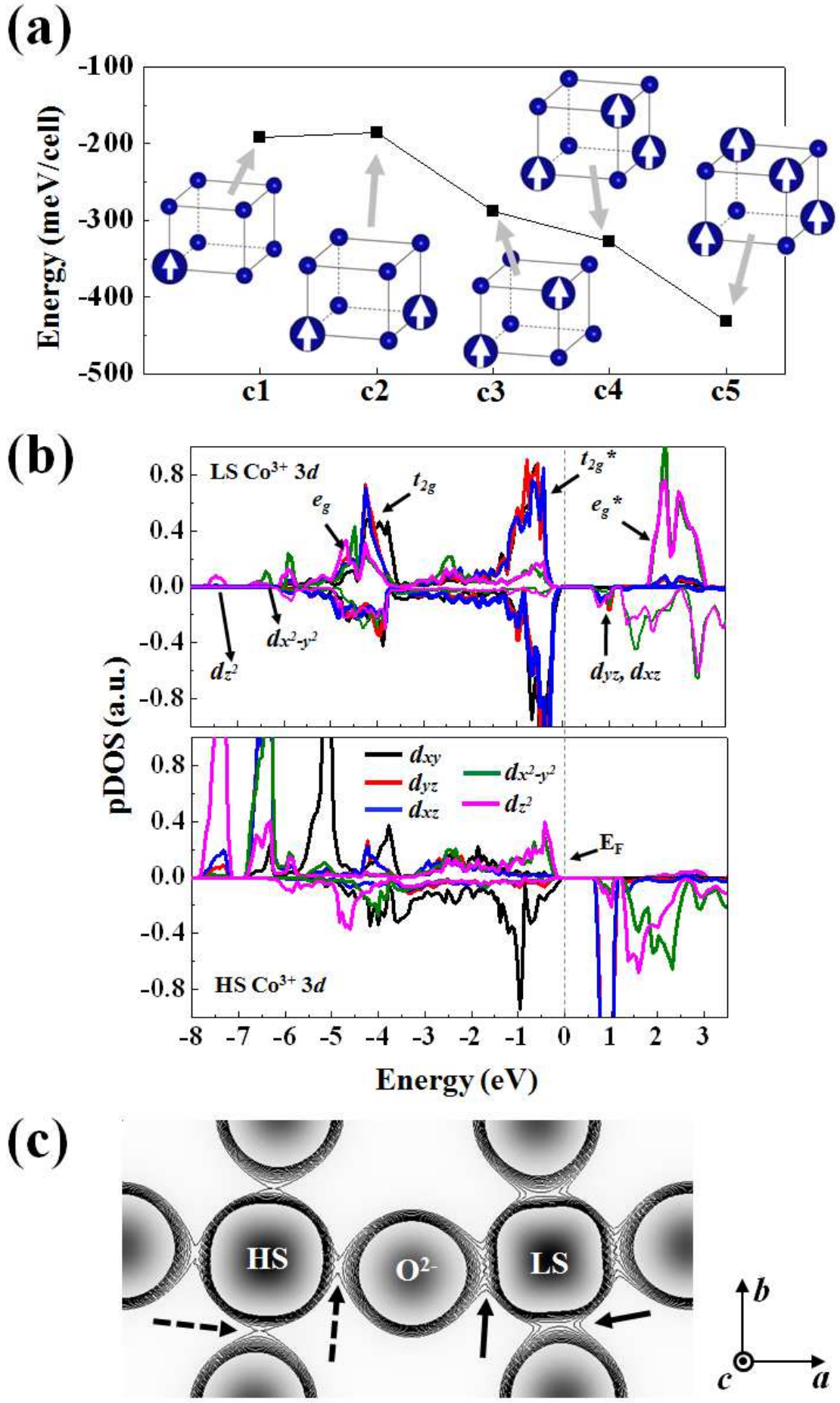

Figure 3 LK12746B 10JUL2012

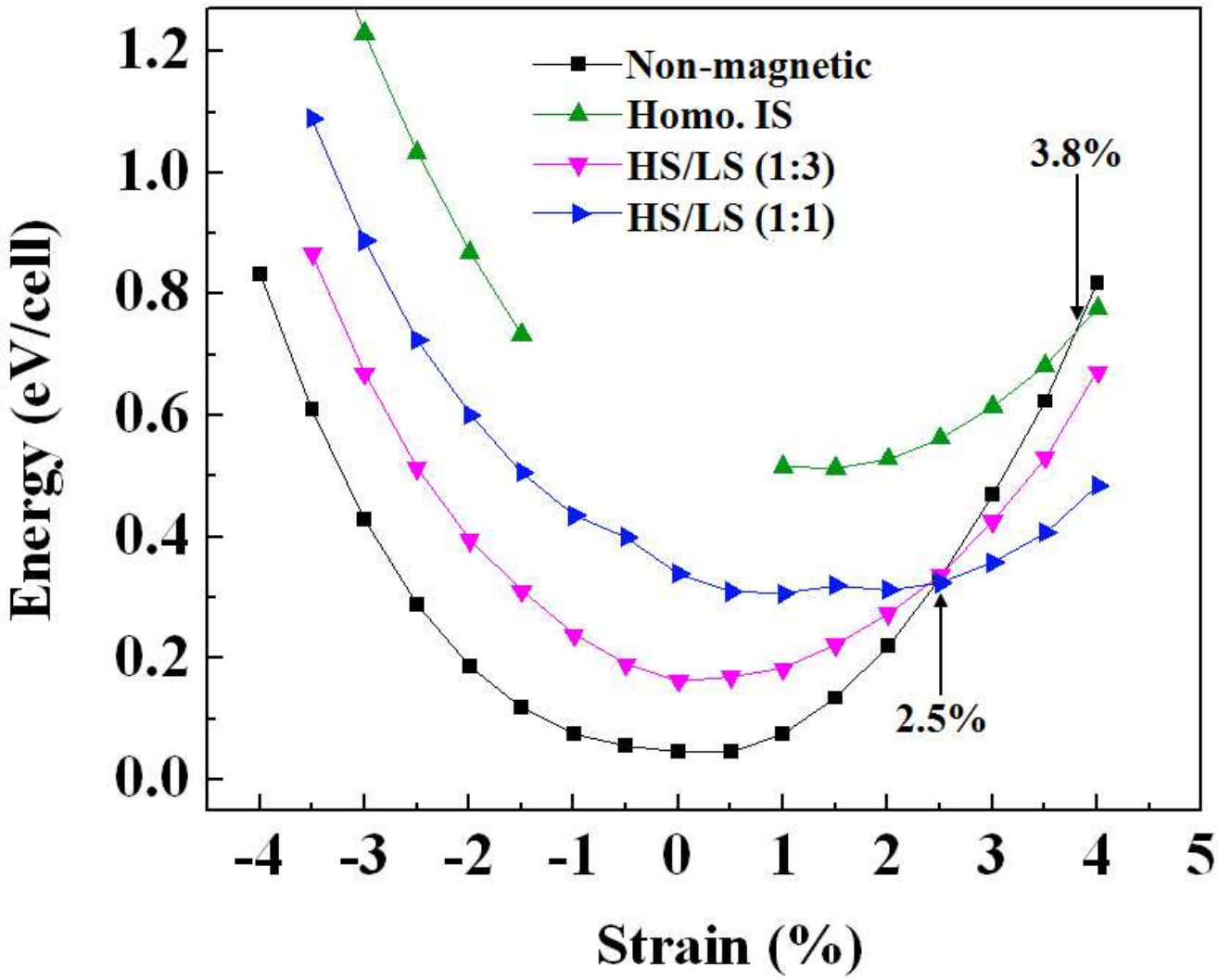

Figure 4 LK12746B 10JUL2012

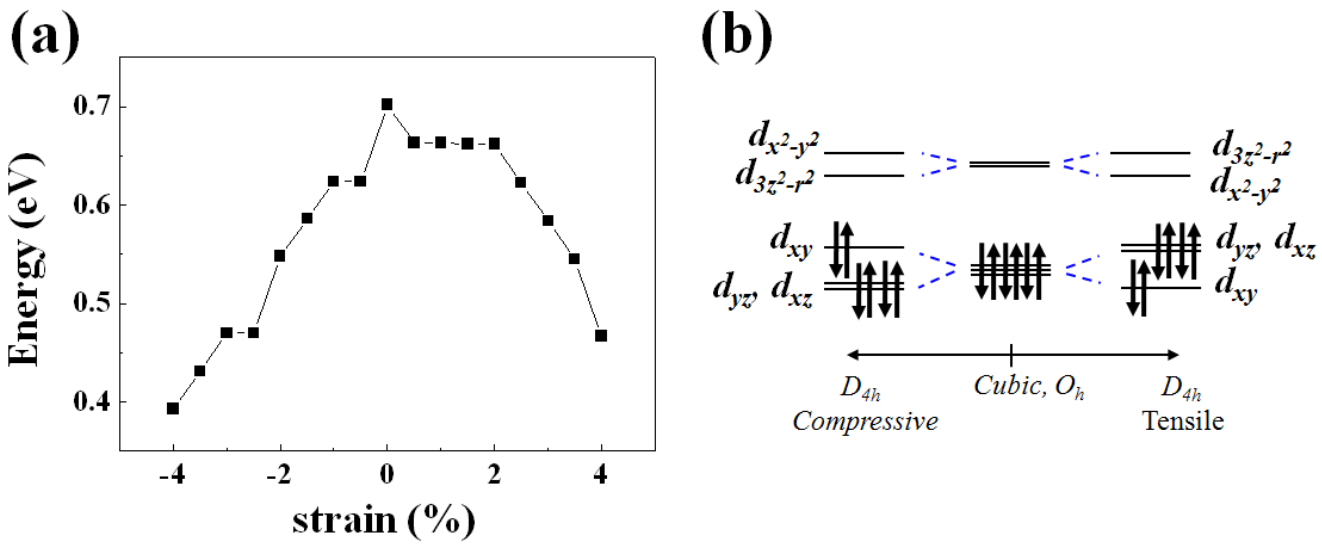

Figure 5 LK12746B 10JUL2012

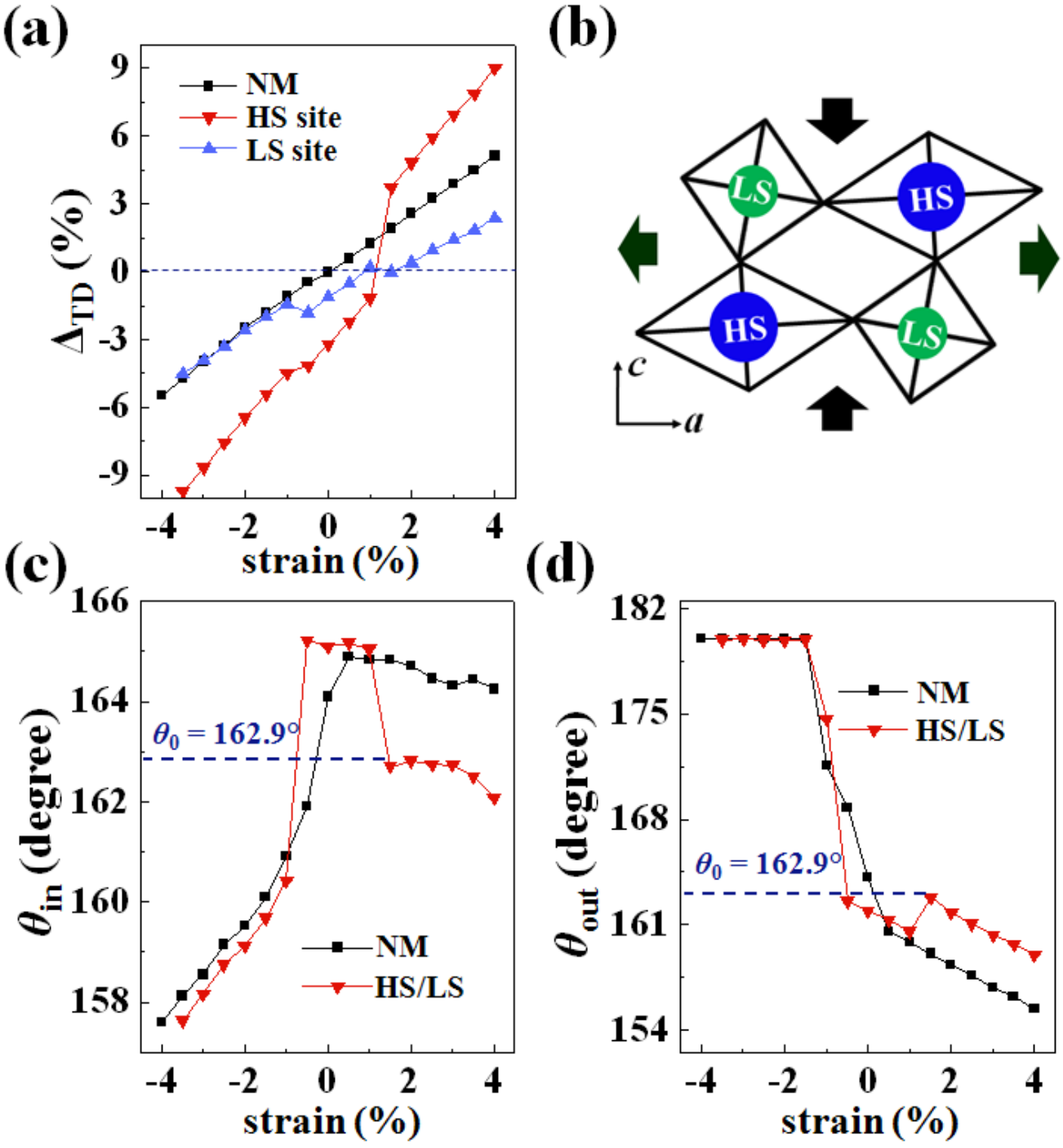

Figure 6 LK12746B 10JUL2012

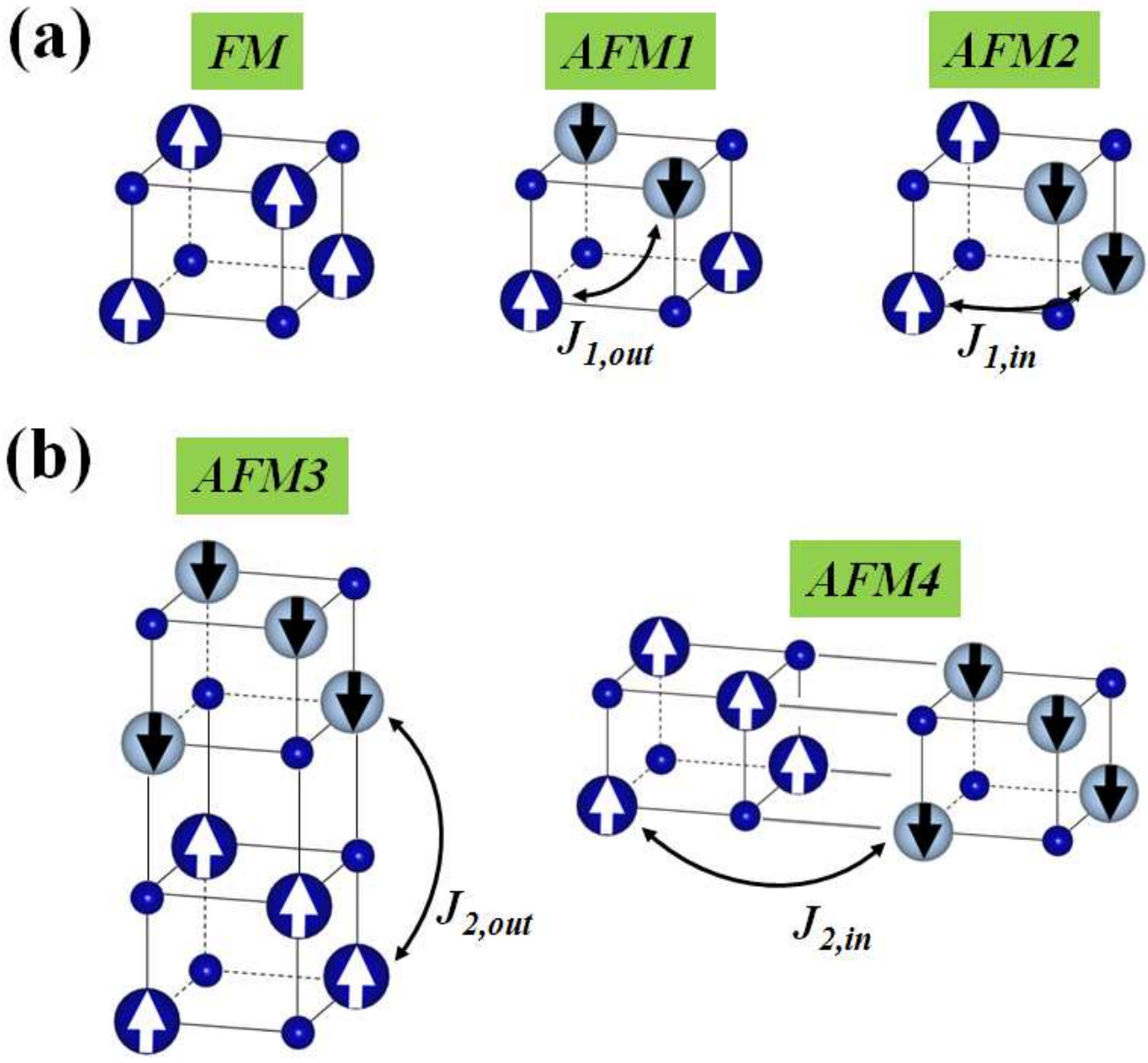

Figure 7 LK12746B 10JUL2012

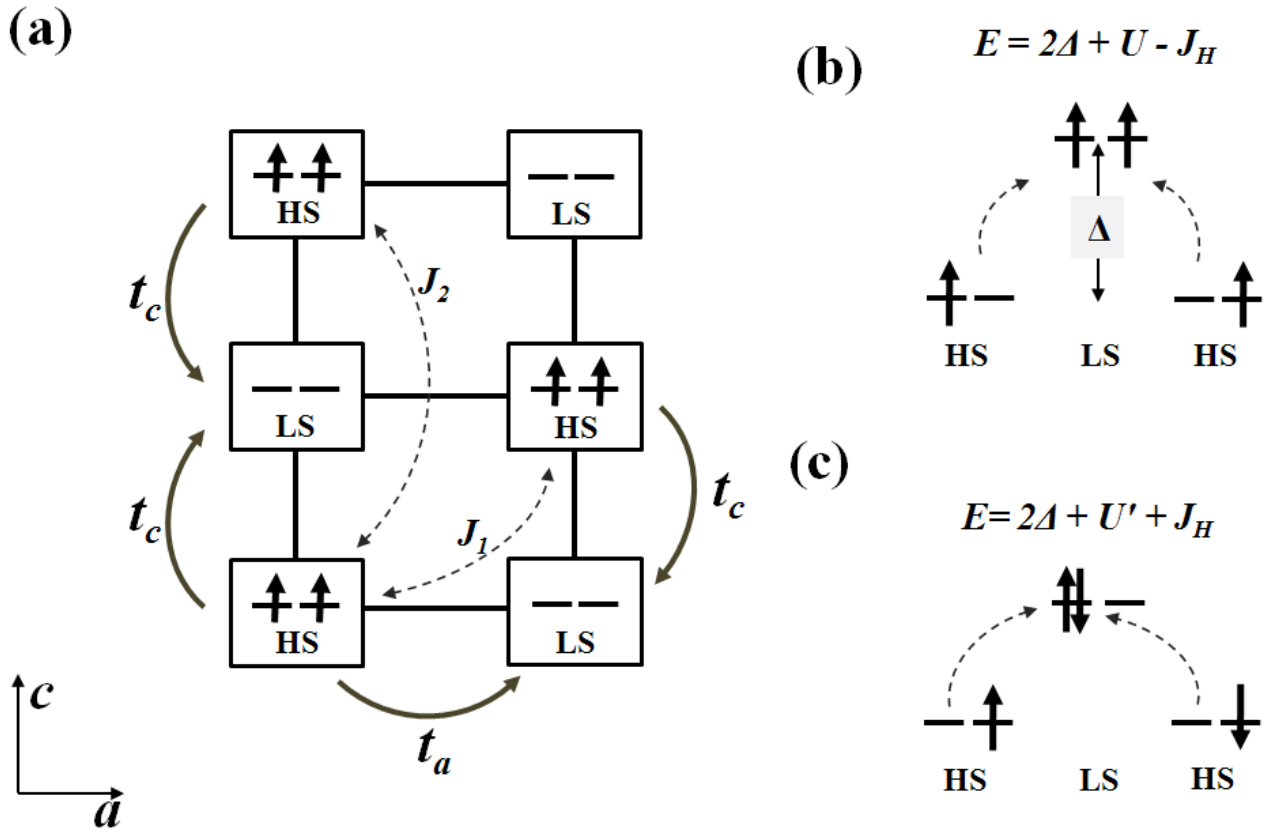

Figure 8 LK12746B 10JUL2012

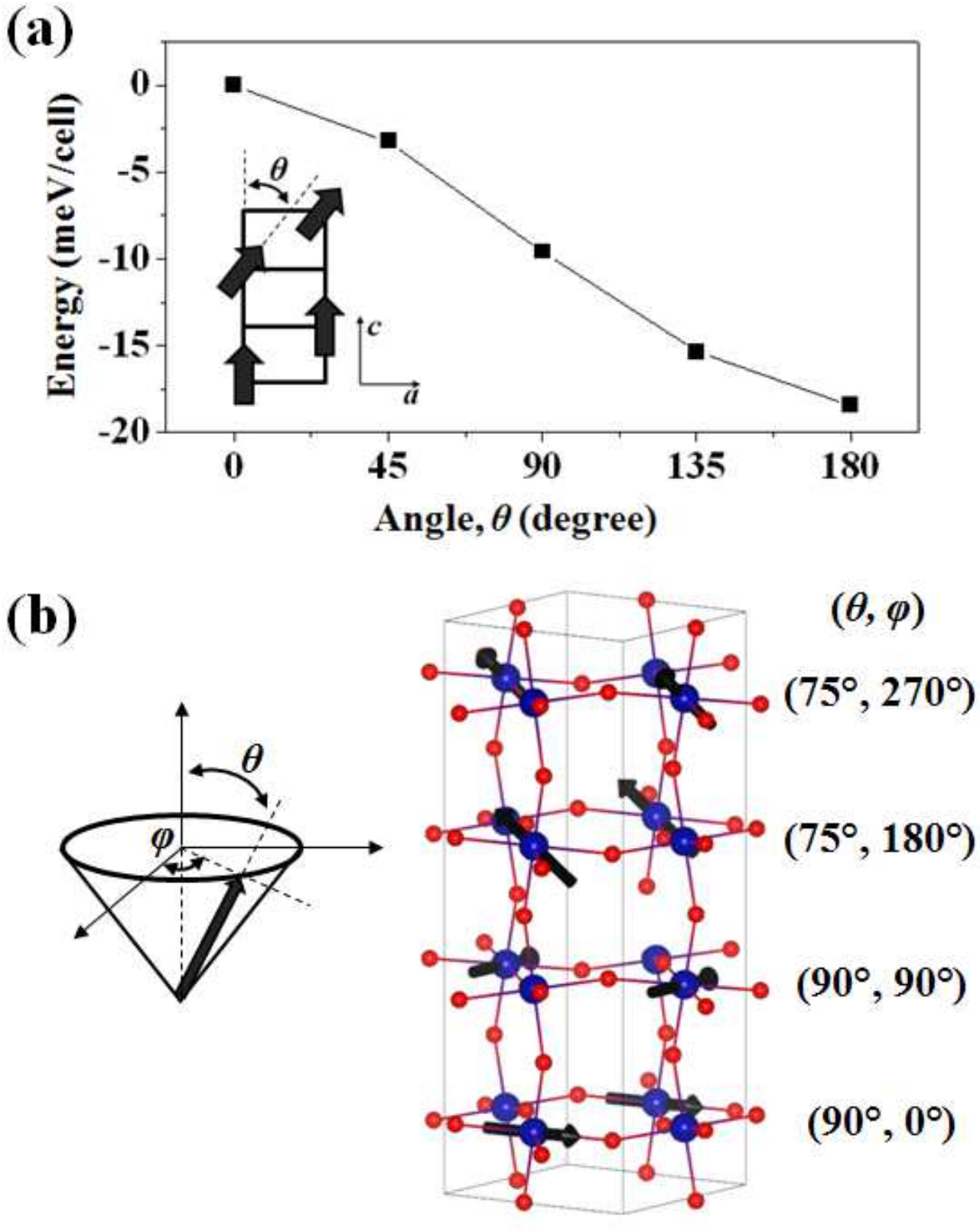

Figure 9 LK12746B 10JUL2012